Effects of solar wind density and velocity variations on the Martian ionosphere and plasma transport—a MHD model study

Yihui Song[1], Haoyu Lu[1,2†], Jinbin Cao[1,2], Xiaoshu Wu[3], Yang Liu[4], Shibang Li[1], Siqi Wang[1], James A. Wild[5], Chenling Zhou[1], Jianxuan Wang[1], Nihan Chen[1]

[1]School of Space and Environment, Beihang University, Beijing, 100191, China

[2]Key Laboratory of Space Environment Monitoring and Information Processing, Ministry of Industry and Information Technology, Beijing, 100191, China

[3]School of Atmospheric Sciences, Sun Yat-Sen University, Zhuhai, China

[4]School of Nuclear Science and Engineering, North China Electric Power University, Beijing, 102206, China

[5]Department of Physics, Lancaster University, Lancaster, UK

†Correspondence to H. Y. Lu at lvhy@buaa.edu.cn

Key Points:

- For constant solar wind pressure, the Martian ionosphere compresses as the solar wind velocity increases.
- For constant dynamic pressure, higher solar wind density leads to higher horizontal ion velocity, facilitating day-to-night transport.
- Strong remnant fields in the southern hemisphere uplift the Martian ionosphere and hinder horizontal ion transport.

Abstract

Solar wind dynamic pressure, consisting solar wind density n_{sw} and velocity V_{sw}, is an important external driver that controls Martian plasma environment. In this study, a 3D magnetohydrodynamic model is applied to investigate the separate influences of solar wind density and velocity on the Martian ionosphere. The spatial distributions of ions in the dayside and near nightside ionosphere under different n_{sw} and V_{sw} are analyzed, as well as the ion transport process. We find that for the same dynamic pressure condition, the ionosphere extends to higher altitudes under higher solar wind density, indicating that a solar wind velocity enhancement event is more efficient at compressing the Martian ionosphere. A higher V_{sw} will result in a stronger induced magnetic field, shielding the Martian ionosphere, preventing the penetration of solar wind particles. For the same dynamic pressure, increasing n_{sw} (decreasing V_{sw}) leads to a higher horizontal ion velocity, facilitating day-to-night plasma transport. As a result, the ionosphere extends farther into the nightside. Also, the ion outflow flux is larger for high n_{sw}, which may lead to a higher escape rate. Moreover, the strong crustal fields in the southern hemisphere also cause significant effect to the ionosphere, hindering horizontal ion transport. An additional outflow channel is also provided by the crustal field on the southern dayside, causing different responses of flow pattern between local and global scale while the solar wind condition is varied.

Plain Language Summary

Solar wind dynamic pressure is one of the main factors that influence Martian space environment. Variation in solar wind velocity and density can cause different effects to the magnetic field and plasma environment in Martian space. By using time dependent 3D multifluid MHD model, we studied the influence of individual solar wind velocity and density on the Martian ionosphere and plasma flow. We found that a higher solar wind density can cause an expansion of ionosphere and a higher outward flow of ions, while a higher solar wind velocity can decrease the horizontal ion velocity and day-to-night transport by enhancing the strength of induced magnetic field, thus the ionosphere extends farther into the nightside under low solar wind velocity condition. The remnant fields of Mars also cause an apparent north-south asymmetry in the ionosphere, since strong crustal fields can deflect plasma flow, hindering horizontal plasma transport while providing an additional vertical outflow channel.

1 Introduction

Mars do not possess an Earth-like global dipole magnetic field. The upstream solar wind interacts directly with the Martian atmosphere/ionosphere, inducing electric currents in the ionosphere, leading to the formation of an induced magnetosphere (e.g., Intriligator, D. S., & Smith, E. J., 1979; Ramstad et al., 2020). The existence of remnant crustal magnetic field located mostly in the southern hemisphere also complicates the interaction process (e.g., Acuña et al., 1998, 1999; Connerney et al., 2015), causing asymmetric structures and plasma flows in the Martian plasma environment (e.g., Fang et al., 2017; Garnier et al., 2022; Harnett & Winglee, 2003, 2005; Li et al., 2020; Li et al., 2023; Stergiopoulou et al., 2022; Wu et al., 2019).

Solar wind dynamic pressure (P_{dyn}), which consists of solar wind density n_{sw} and velocity V_{sw}, is one of the most important external drivers that controls the variation of Martian space environment (e.g., Edberg et al., 2009; Nagy et al., 2004). Previous studies have proved that an enhancement of the solar wind dynamic pressure can compress the plasma boundaries to lower altitudes, alter the global magnetic topology, and increase the magnitude of magnetic forces and ion escape rates (e.g., Chu et al., 2021; Dong et al., 2015; Duru et al., 2020; Garnier et al., 2017; Ma et al., 2014; Song et al., 2023; Weber et al., 2019; Xu et al., 2018). However, the relative influences of solar wind velocity and density variations on the Martian plasma environment have seldomly been discussed separately, and the differences between the impacts caused by the solar wind density and velocity variation on the Martian plasma environment still need to be studied systematically. The simulation study of Wang et al. (2021) shows that for constant P_{dyn}, a lower n_{sw} can increase the subsolar distance of the Martian magnetic pileup boundary (MPB) and decrease that of the bow shock (BS), while Ramstad et al. (2017) and Wang et al. (2020) reported that the location of BS and MPB are controlled by P_{dyn} rather than individual solar wind velocity/density. Ramstad et al. (2015) also found that for the same solar wind velocity, a lower solar wind density (lower P_{dyn}) may increase the ion escape rate, which is contradictory to the conclusion of numerous literatures (e.g., Dong et al., 2015; Edberg et al., 2010; Kaneda et al., 2007; Ma et al., 2014, 2017). In addition, previous studies have focused on the influences of individual solar wind velocity/density variation on Martian boundary layers and ion escape, leaving the response of Martian ionosphere undiscussed.

The primary source of plasma in the dayside ionosphere of Mars is the photoionization process (Withers et al., 2009). However, on the nightside, despite lack of the solar radiation, a weak and sporadic ionosphere is produced there, mainly through trans-terminator plasma transport and electron precipitation (Zhang et al., 1990). The impact of solar radiation on the Martian ionosphere does not vanish until the solar zenith angle (SZA) is approximately $105°$, thus the nightside ionosphere can be divided into the near-terminator region ($90° < \mathrm{SZA} < 105°$) and the dark ionosphere ($\mathrm{SZA} > 105°$). The plasma day-to-night transport, which is strongly influenced by the dayside ionosphere, functions as a main source in the regions with $\mathrm{SZA} < 115°$ in the nightside(Cao et al., 2019; Cui et al., 2015; Withers et al., 2012(a)), while electron precipitation controls the regions with $\mathrm{SZA} > 115°$ (e.g., Cui et al., 2019; Girazian et al., 2017). In addition, Němec et al. (2010) reported that the influence of plasma transport on the nightside ionosphere does not terminate until $\mathrm{SZA} = 125°$, since the occurrence rate of nightside ionosphere identified in ionograms decreases with increasing SZA up to $\mathrm{SZA} = 125°$.The main peaks in nightside ionospheric plasma density are observed between 120 and 180 km, with the peak electron density roughly 1-2 orders of magnitude lower than that on the dayside (e.g., Fowler et al., 2015; Girazian et al., 2017; Lillis et al., 2009).

Both the dayside and nightside Martian ionosphere can be compressed and experience much heavier erosion under high solar wind dynamic pressure conditions (e.g., Dubinin et al., 2018; Girazian et al., 2019; Ma et al., 2014). Previous observations have shown that during solar wind enhancement events, the nightside ionosphere will be significantly enhanced at lower altitudes, with the peak electron densities increased by enhanced electron impact ionization (Harada et al., 2018). Dieval et al. (2014) found that the nightside ionospheric peak densities increase for enhanced upstream dynamic pressures, similar to the dependency shown on Venus (Zhang et al., 1990). Nevertheless, Girazian et al. (2019) and Dubinin et al., (2019) shows that the topside nightside ionosphere experienced a stronger erosion at all SZAs and all altitudes under high solar wind dynamic pressure conditions, indicating the reduction of plasma transport or impact ionization or both. However, none of these studies analyzed how solar wind dynamic pressure variation systematically affects the nightside ionosphere through plasma transport process. Moreover, the dominant driver of day-to-night ion transport remains unclear. Chaufray et al. (2014) reported a distinct difference of trans-terminator ion velocity between thermospheric model results and observations, suggesting that the solar wind could be the main driver of trans-terminator flow, while Hamil et al. (2019) revealed that magnetic pressure gradient dominates day-to-night flow.

Since the in-situ observations are intrinsically limited by temporal and spatial sampling coverage, the global ionospheric structures reveal by observational data are usually averaged across long time intervals, during which multiple external parameters such as the solar wind condition and interplanetary magnetic field may change dramatically. The mixture of multiple parameters complicates the interaction between solar wind and Mars, which makes it challenging to distinguish consequences caused by the variation of individual solar wind density and velocity parameters. Therefore, in order to investigate the impact of solar wind density/velocity variation on the Martian plasma environment thoroughly, studies based on global simulation models and ideal solar wind condition inputs are necessary. Numerous numerical models have been used to study solar system plasma, including magnetohydrodynamic model (MHD), test-particle model and hybrid model (Ledvina et al., 2008). The MHD model commonly used in the simulation of Martian plasma environment can also be divided into single-fluid MHD model, which assumes that all the ion species have the same velocity and temperature (Ma et al., 2014), and multi-fluid MHD model, which solves mass, momentum and energy equations separately for each ion species (Najib et al., 2011).

In this study, we study six simulation cases with the ideal solar wind parameter setting to investigate the influence of n_{sw} and V_{sw}, respectively, on the Martian nightside ionosphere. By using 3D multi-fluid MHD model, we first compared the nightside electron density profile under constant P_{dyn} conditions but with differing n_{sw} and V_{sw} inputs, then the possible mechanisms are discussed by analyzing ion transport flows. The rest of the paper is organized as follows: a detailed model description is presented in Section 2, simulation results are shown in Section 3, while Section 4 provides the conclusion of our study.

2 Model description

In this study, a 3D multi-fluid MHD model that has been used and validated in several previous studies (e.g., Li et al., 2022a; 2022b, Song et al., 2023) is applied to simulate the interaction between solar wind and the Martian ionosphere/induced magnetosphere. Four major ion species in Martian ionosphere, i.e., H^+, O_2^+, O^+, and CO_2^+, are included in the model. The ion species are self-consistently generated through ionospheric chemical reactions including photoionization, charge exchange and recombination reactions (Ma et al., 2004; Najib et al., 2011). The chemical reactions used in the model are presented in Table 1, with the reaction rates for solar maximum conditions derived from Ma et al. (2004). The three main neutral components in the Martian atmosphere are considered in the model, with the 1-D neutral density profile used in Li et al. (2022a). The Chapman function is used instead of the cosine function of solar zenith angle to derive the optical depth effect, which can describe the M2 layer more precisely (Withers et al. 2009). The MHD equations used in the model consist of the continuity, momentum and energy equations as well as a magnetic induction equation in which the Hall term and thermal pressure gradient term are considered. The source terms considered in the MHD equations include inelastic collisions (charge exchange, recombination and photoionization) and elastic collisions (ion-neutral and ion-ion collisions). A detailed description of the MHD model can be found in Song et al. (2023)

Table 1. *Chemical reactions and rates considered in the model.*

Reaction	Rate Coefficient
$CO_2 + h\nu \rightarrow CO_2^+ + e^-$	$k_1 = 7.3 \times 10^{-7} s^{-1}$
$O + h\nu \rightarrow O^+ + e^-$	$k_2 = 2.73 \times 10^{-7} s^{-1}$
$H + h\nu \rightarrow H^+ + e^-$	$k_3 = 8.59 \times 10^{-8} s^{-1}$
$CO_2^+ + O \rightarrow O_2^+ + CO$	$k_4 = 1.64 \times 10^{-10} cm^3 s^{-1}$
$CO_2^+ + O \rightarrow O^+ + CO_2$	$k_5 = 9.6 \times 10^{-11} cm^3 s^{-1}$
$O^+ + CO_2 \rightarrow O_2^+ + CO$	$k_6 = 1.1 \times 10^{-9} (800/T_i)^{0.39} cm^3 s^{-1}$
$O^+ + H \rightarrow H^+ + O$	$k_7 = 6.4 \times 10^{-10} cm^3 s^{-1}$
$H^+ + O \rightarrow O^+ + H$	$k_8 = 5.08 \times 10^{-10} cm^3 s^{-1}$
$O_2^+ + e \rightarrow O + O$	$k_9 = 7.38 \times 10^{-8} (1200/T_e)^{0.56} cm^3 s^{-1}$
$CO_2^+ + e \rightarrow CO + O$	$k_{10} = 3.1 \times 10^{-7} (300/T_i)^{0.35} cm^3 s^{-1}$

The simulation was performed under the Mars-centered Solar Orbital (MSO) coordinate system. The X-axis points from Mars toward the Sun, the Z-axis points toward the north pole of Mars and is normal to the Martian orbital plane, while the Y-axis completes the right-handed coordinate system. The computational domain is defined as $-24R_M \leq X \leq 8R_M$, $-16R_M \leq Y$ and $Z \leq 16R_M$, where R_M represents the average radius of Mars ($R_M \approx 3396$ km). The mesh used in the model consists 56 blocks and $100 \times 120 \times 80 = 960{,}000$ computational cells, with the smallest grid size set to be 10 km at the inner boundary (100 km above the Martian surface). The density and velocity of H^+ at the inner boundary is set to be 0.3 of the solar wind density and zero (derived from Dong et al. (2014)), respectively, while the ion densities are assumed as the photochemical equilibrium. A $110°$ spherical harmonic crustal field model proposed by Gao et al. (2021) was adopted in our model to simulate the Martian remnant magnetic field, with the most intense magnetic field locates at $-53°$ latitude. The subsolar point is set to be $180°$ longitude at equatorial plane, meaning that the strongest crustal field regions are located on the dayside.

The upstream solar wind conditions in the 6 cases-studies considered in this work are shown in Table 2. In this way, the effects of solar wind dynamic pressure with different solar wind velocity and density on the nightside ionosphere were studied. We utilize two sets of dynamic pressure conditions P_{dyn} = 1.07 and 4.28 nPa and three sets of solar wind density conditions n = 2, 4, 8 cm^{-3} for each P_{dyn} set, enabling the comparison of the influence of individual n_{sw} and V_{sw} variation for two different P_{dyn} conditions. The interplanetary magnetic field (IMF) is set to be a $56°$ Parker spiral in the X-Y plane, meaning that the IMF vector is $(B_x, B_y, B_z) = (-1.6, 2.5, 0)$ nT in MSO coordinate system. The upstream solar wind velocity is purely in the -X direction, with V_Y and V_Z set to be zero.

Table 2. *Upstream solar wind condition settings of simulation cases.*

	V_X (km/s)	n (cm^{-3})	P_{dyn} (nPa)	$\lvert B \rvert$ (nT)	T_p (K)
Case 1	566	2	1.07	3	3.5×10^5
Case 2	400	4	1.07	3	3.5×10^5
Case 3	283	8	1.07	3	3.5×10^5
Case 4	1131	2	4.28	3	3.5×10^5
Case 5	800	4	4.28	3	3.5×10^5
Case 6	566	8	4.28	3	3.5×10^5

3 Simulation results

We first compare the density distributions of the dayside and near nightside ionosphere under different solar wind conditions. The mean ionospheric electron density (n_e) profiles at different SZA ranges are shown in Figure 1. Here we choose to present SZA ranges from $80°$ to $120°$, since at regions with SZA $< 115°$, day-to-night plasma transport is the dominant plasma source of the nightside ionosphere, while at higher solar zenith angles, electron precipitation becomes the main source (Cui et al., 2015; Qin et al., 2022a; Withers et al., 2012a).

From Figure 1, it can be seen that the peak electron densities decrease with increasing SZA for all cases (see Figure 1(c)-1(d) for a clear comparison). Under low P_{dyn} conditions (see Figure 1(a)), the peak electron densities decrease from around $10^{4.5}$ e$^-$/cm^3 at SZA region $80° - 90°$ to around 10^3 e$^-$/cm^3 at SZA region $110° - 120°$, varying by more than an order of magnitude. The magnitude of peak electron densities does not show a clear north-south asymmetry. Nevertheless, at altitudes above 300 km, the density profiles in the southern hemisphere are slightly uplifted for SZA range $80° - 100°$, compared to that of the northern hemisphere, indicating an expansion of the southern ionosphere in the terminator region. The expansion of the ionosphere in the southern hemisphere may be caused by the shielding effect of strong crustal fields. As for SZA range $100° - 120°$, the density profiles are uplifted in the northern hemisphere than that in the south, which may be caused by the differences of plasma transport between the northern and southern hemisphere. In addition, previous studies have shown that convection electric field can also cause a distinct asymmetry of the Martian upper ionosphere, causing the expansion of ionosphere in the hemisphere that is opposite to the direction of motional electric field (E^- hemisphere) (Dubinin et al., 2018). In our model the MSE coordinate system is the same as the MSO coordinate system, thus the E^+ direction, which is the direction of motional electric field, is parallel to the Z axis in MSO coordinate system.

Therefore, the convection electric field also contributes to the south-north asymmetry shown in the model results.

While the P_{dyn} condition remains the same, the mean electron densities at all altitudes and all SZA ranges increase with increasing n_{sw} (decreasing V_{sw}). For SZA range $80° - 100°$, the inflation of electron density profiles only appears at higher altitudes, while for SZA range $100° - 120°$, the difference occurs at all altitude above 110 km. Thus, it can be concluded that the decrease of peak densities with increasing SZA is less significant for higher n_{sw} conditions, indicating that the high n_{sw} cases may be associated with more efficient day-to-night plasma transport. For high P_{dyn} conditions, as shown in Figure 1(b), the density peaks of SZA $100° - 120°$ ranges migrate to lower altitudes, and the magnitudes of the density peaks are slightly enhanced. Comparing to low P_{dyn} conditions, the averaged electron density at altitudes 200 – 400 km experienced an apparent depletion for all SZAs, consistent with previous findings of Girazian et al. (2019).

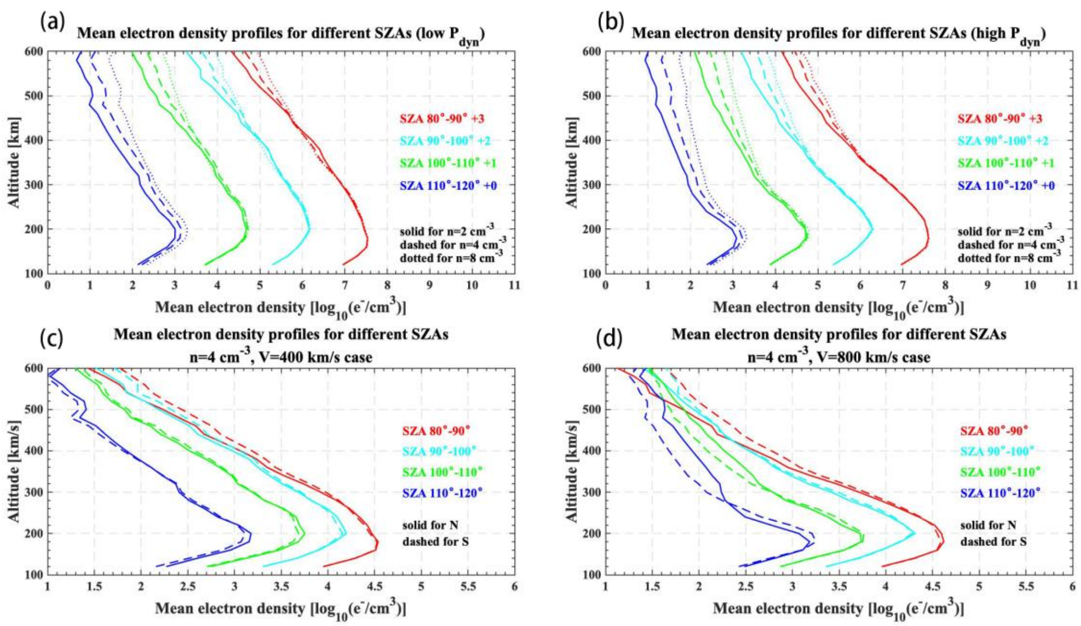

Figure 1. The mean electron density profiles for different SZA range in the terminator region. Panels a and b show the averaged electron density profiles under low P_{dyn} conditions and high P_{dyn} conditions. The solid, dashed and dotted line represent profiles of $\mathrm{n} = 2\ \mathrm{cm}^{-3}$ cases, $\mathrm{n} = 4\ \mathrm{cm}^{-3}$ cases, $\mathrm{n} = 8\ \mathrm{cm}^{-3}$ cases, respectively. The profiles are shifted on the x-axis by the amounts marked in the figure. Panels c and d show the averaged electron density profiles of case 2 and case 5, with solid and dashed line represents profiles of northern and southern hemisphere.

To illustrate how solar wind conditions and crustal field affect the expansion and shrinking of dayside and near nightside ionosphere, Figure 2 and 3 present the mean electron density and the upper boundary of ionosphere for low and high solar wind dynamic pressure conditions respectively. These figures correspond to the SZA range between $0° - 120°$ with a bin-size of $5°$ and to the altitude range 120-600 km with a bin-size of 20 km. The isoelectron-density lines for $n_e = 100\ \mathrm{cm}^{-3}$ are highlighted by white lines in panel a and c, representing the ionospheric upper boundary locations (Ma et al., 2014). The upper boundaries of ionosphere in panel b and d are derived in the same way as in panel a and c. Note that the ionospheric upper boundary defined here is not the ionopause, which is generally identified by the sudden decrease of the ionospheric electron density with increasing altitude or pressure balance criterion (Sanchez-Cano et al., 2020), but an indication of approximately how far the ionosphere extends. Here we use a defined ionospheric upper boundary instead of the ionopause, partly because the Martian ionopause is sporadic and not always been observed (Chu et al., 2019; Duru et al., 2009; 2020; Vogt et al., 2015).

For low P_{dyn} condition cases (see Figure 2), the ionosphere on the dayside and near terminator region (SZA range $0° - 100°$) in the southern hemisphere extends to higher altitudes compared to the ionosphere in the northern hemisphere, consistent with the results reported in previous studies that the Martian ionosphere is uplifted over strong crtustal field regions (e.g., Andrews et al., 2023; Dubinin et al., 2019; Flynn et al., 2017; Withers et al., 2019). However, at SZA $\sim 120°$, significant differences in the altitude of the ionospheric upper boundary between the northern and southern hemisphere are not evident. The upper boundary of ionosphere on the dayside locates at 400-600km, which is in the altitude range of observed average ionopause location (300-600 km) (Withers et al., 2012b; Duru et al., 2020), and coincide with the upper ionospheric boundary predicted by Ma et al. (2014) using the same criterion. For both the northern and southern hemispheres, the upper boundary of the ionosphere reaches the highest point near the terminator, then decreases sharply with the increasing SZA on the nightside, fitting well with the distribution of ionospheric ions shown by Dubinin et al. (2019) and Andrews et al. (2023).

Comparing the different scenarios, it can be clearly seen that for constant P_{dyn}, the upper boundary of ionosphere extends to higher altitudes with increasing n_{sw} (see Figure 2(b) and 2(d)) in both the dayside and near nightside regions. Since the plasma transport process does not generate new particles on a global scale, the uplifting of the ionosphere in SZA range $0° - 120°$ may be caused by a more intense impact ionization process. Under high solar wind density conditions, more solar wind particles enter the Martian ionosphere, interacting with ionospheric plasmas and neutral components, leading to a higher production rate of ionospheric ions. The expansion of nightside ionosphere in high n_{sw} case may also be partly caused by the difference of day to night plasma transport for different solar wind conditions, since the near nightside region is dominated by transportation instead of precipitation processes.

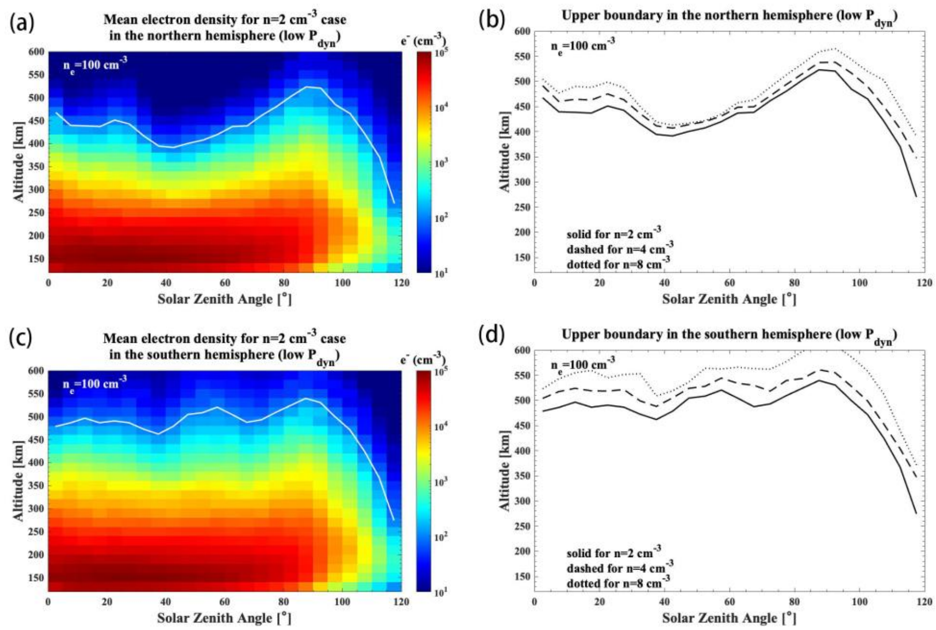

Figure 2. Panels a and c show the mean electron density of Martian ionosphere for an SZA range of $0° - 120°$ and an altitude range of 120-600 km for low P_{dyn} condition cases, divided into the northern (panel a) and southern (panel c) hemisphere. The white line in each panel marks the altitudes that the electron density n_e is equal to 100 cm^{-3}. Panels b and d show the ionospheric upper boundary in the northern (panel b) and southern (panel d) hemispheres separately, with the solid, dashed and dotted line represent the boundary of $\text{n} = 2 \text{ cm}^{-3}$ case, $\text{n} = 4 \text{ cm}^{-3}$ case, $\text{n} = 8 \text{ cm}^{-3}$ case, respectively.

Under enhanced P_{dyn} conditions (see Figure 3), the ionosphere in all three cases experienced an apparent compression at dayside and near terminator region. However, in regions with SZA $\sim 120°$, the locations of ionospheric upper boundary seldomly move compared to that for low P_{dyn} condition cases, indicating that the depletion effect of high P_{dyn} in the Martian ionosphere is weak at regions with SZA $> 120°$. In the high P_{dyn} condition cases, the ionosphere also expands to higher altitudes with increasing n_{sw}, same as in the low P_{dyn} condition cases. By comparing case 1 (Figure 2(b) and 2 (d)), case 4 and case 6 (Figure 3(b) and 3(d)), it can also be concluded that the enhancement of solar wind velocity compresses the Martian ionosphere to lower altitudes more effectively than the enhancement of solar wind density. The nightside upper boundary of ionosphere even expands in case 6 compared to case 1, indicating that the expansion effect caused by the higher solar wind density condition and the stronger day-to-night transport surpasses the compression effect caused by the enhanced P_{dyn} in this region. Therefore, it can be concluded that the solar wind velocity enhancement event is more efficient at compressing dayside ionosphere compared to solar wind density enhancement event, but in nightside region the scenario is much more complicated, for the variation of solar wind conditions also influences plasma transport processes.

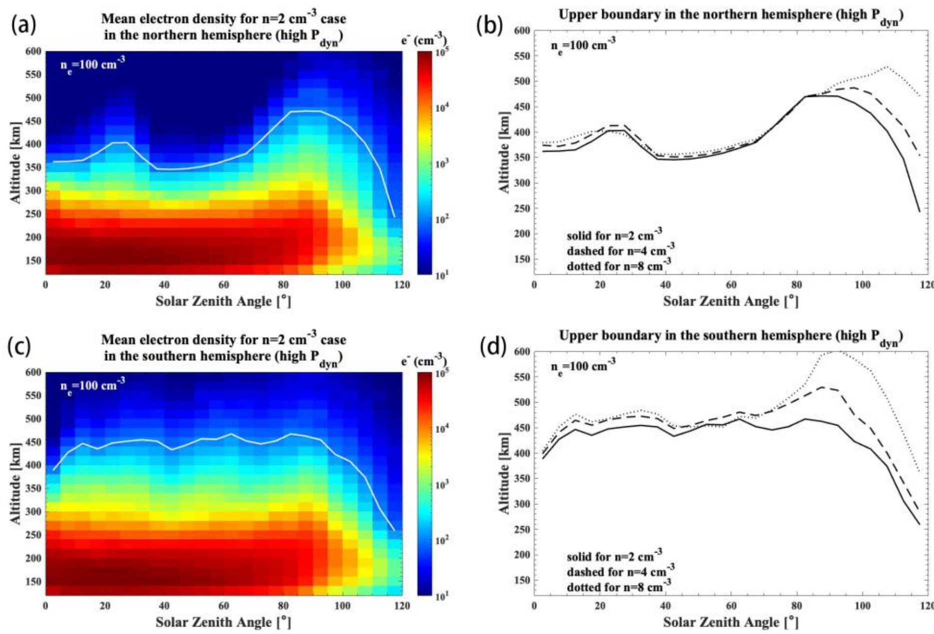

Figure 3. Panels a and c show the mean electron density of the Martian ionosphere for an SZA range of $0° - 120°$ and an altitude range of 120-600 km for high P_{dyn} condition cases, divided into the northern (panel a) and southern (panel c) hemispheres. The white line in each panel marks the altitudes that the electron density n_e is equal to $100\ \mathrm{cm}^{-3}$. Panels b and d show the ionospheric upper boundary in the northern (panel b) and southern (panel d) hemispheres separately, with the solid, dashed and dotted line represent the boundary of $\mathrm{n} = 2\ \mathrm{cm}^{-3}$ case, $\mathrm{n} = 4\ \mathrm{cm}^{-3}$ case, $\mathrm{n} = 8\ \mathrm{cm}^{-3}$ case, respectively.

To illustrate how solar wind density/velocity influence the day-to-night transport process, we show the "1/e profile" of heavy ion and electron density in Figure 4, with respect to altitude range 100-600 km. The 1/e edge (with e being the base of natural logarithms) is defined as where the ion/electron density declines to 1/e of that at SZA=90°, characterizing the depletion of nightside ionosphere (Cao et al., 2019). It should be noted that the 1/e edge values in Figure 4 and the iso electron-density lines in Figure 2 and 3 are obtained from the interpolation method.

In Figure 4, the 1/e edge profiles of the southern/northern hemisphere under different solar wind condition settings are compared, showing the influence of solar wind velocity/density and the crustal fields upon ion depletion in the nightside ionosphere. In the altitude range 150-250 km, the 1/e edge of O_2^+ and CO_2^+ typically appears in the SZA range $95° - 105°$, similar to the observational results of Cao et al. (2019). Under 200 km, the 1/e edge profiles of different cases and hemispheres do not show clear differences, since the transport process becomes important at altitudes above 200 km. The 1/e edge of O^+ extends to much larger SZA range than that of O_2^+ and CO_2^+, indicating that the ion distribution of O^+ is more extended into nightside as compared to other heavy ion species. As ion depletion in the nightside ionosphere is influenced by the ion chemical loss process, such a phenomenon can be interpreted by the relatively lower reaction rate of the chemical loss reaction of O^+ considered in our model. Such discrepancy may also be caused by the difference of ion speed, a higher velocity can transport ions to the regions with larger SZA. However, we do not compare the efficiency of day-to-night transport for different heavy ions here, as this is beyond the scope of the current study.

By comparing 1/e edge profiles of the northern/southern hemisphere under different solar wind conditions, two distinctive features can be seen. Compared to the southern hemisphere, the 1/e edges of the northern hemisphere are extend further into the nightside for all four ion species and cases analyzed here, similar to the results reported by Cao et al. (2019). Since in our model the strongest region of crustal field is fixed on the dayside, this phenomenon may be mainly caused by the ion transport process instead of the protection effect of strong crustal fields on the nightside ionosphere. The 1/e profiles also show apparent distinctions for different solar wind conditions. With the increase of n_{sw} and the decrease of V_{sw}, the ion distribution in both hemispheres extends into regions with higher SZA, coinciding with the uplifted nightside ionospheric upper boundary shown in Figure 2-3. It is reasonable to deduce that a higher n_{sw} condition can facilitate ion transport to the nightside ionosphere, while the strong remnant fields retard this process.

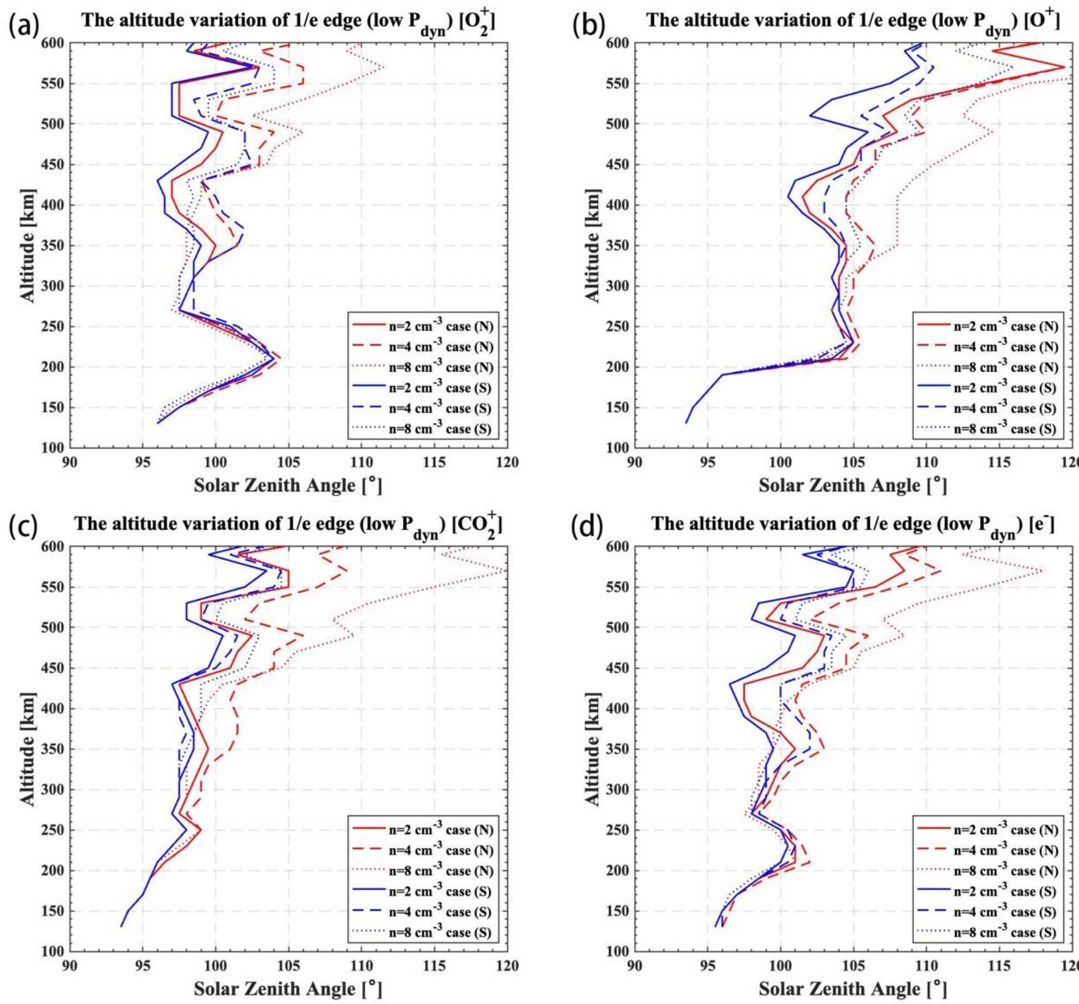

Figure 4. The 1/e edge profile of density with respect to altitude and SZA of O_2^+ (panel a), O^+ (panel b), CO_2^+ (panel c) and e^- (panel d) for low P_{dyn} condition. The 1/e edge is defined as the

SZA where the ion/electron density declines to 1/e of the magnitude at the terminator (SZA=90°). Red and blue line show the profiles of the northern and the southern hemisphere, respectively, while solid, dashed and dotted line represent $\mathrm{n} = 2\ \mathrm{cm}^{-3}$ case, $\mathrm{n} = 4\ \mathrm{cm}^{-3}$ case and $\mathrm{n} = 8\ \mathrm{cm}^{-3}$ cases, respectively.

Profiles of the mean trans-terminator velocity of O_2^+ ions along x-axis (V_X) with respect to altitude are presented in Figure 5, with the positive direction in this figure corresponding to the -X direction. For both low P_{dyn} and high P_{dyn} conditions, the trans-terminator velocity in the northern hemisphere is significantly higher as compared to that in the southern hemisphere, showing that the suppression effect of the dayside strong crustal fields on plasma transport can influence the ion velocity at the terminator region, leading to north-south asymmetry of the trans-terminator plasma flow. For low P_{dyn} conditions, the average V_X at 400 km in the southern hemisphere is 450-700 m/s, while in the northern hemisphere the magnitude is 900-1200 m/s.

Under low P_{dyn} condition (see Figure 5(a)), the magnitude of V_X is significantly larger for the high n_{sw} case, indicating that higher solar wind density condition can facilitate day-to-night plasma transport. Considering that the plasma density near terminator region is also denser for higher n_{sw} condition, it is reasonable to deduce that the trans-terminator ion flux for high n_{sw} condition case is also greater than that of the low n_{sw} condition case. Thus, we conclude that the higher electron density and more expanded ionosphere in near nightside for high n_{sw} condition is partly caused by the stronger trans-terminator plasma flow. In addition, it can be clearly seen that the discrepancy of V_X for different cases is more significant in the southern hemisphere as compared to that in the northern hemisphere, which may be caused by the shielding effect of the crustal fields.

For high P_{dyn} conditions, the magnitude of V_X experiences a significant enhancement at all altitudes. At 400 km, the average V_X in the southern hemisphere reaches 2000 m/s, about four times greater than that for low P_{dyn} condition, while in the northern hemisphere the magnitude of that reaches 4000 m/s. The velocity profiles of high P_{dyn} cases do not show clear differences in the northern hemisphere. In the southern hemisphere, the magnitude of V_X is larger for high n_{sw} condition at altitude range 200-400 km, however, above 400 km this trend is gradually reversed. The inverse correlation between V_X and n_{sw}/V_{sw} above 400 km maybe caused by the discrepancy of the ionospheric topside boundaries in different cases. The upper ionospheric boundary is located at 450 km for case 4, but extends to above 500 km for cases 5 and 6. Thus, in the case with low n_{sw} condition, the ionospheric plasma is obviously experiencing a stronger impact from the solar wind as compared to other two cases, resulting in a higher ion transport velocity above 450 km. Nevertheless, since plasma density near the terminator region is still larger for high n_{sw} condition case, the trans-terminator flux should also be larger even though the magnitude of velocity term is approximately the same for each case. Also, as plasma density is much lower above 450 km compared to that at 200-450 km, the total trans-terminator ion flux in the ionosphere should still be higher for high n_{sw} case in general.

As the discrepancy of V_X for different n_{sw} and V_{sw} conditions remains in low altitude of the southern hemisphere, but completely disappears in all altitudes of the norther hemisphere, we suspect that this correlation is not caused by the direct interaction of solar wind plasma and ionospheric ions, but result from more complex energy transfer processes. The study by Wang et al. (2021) indicates that for constant P_{dyn} condition, a higher V_{sw} (lower n_{sw}) results in a stronger magnetic pileup region and a higher MPB altitude. In this way, the shielding effect of the induced magnetosphere is stronger, suppressing the energy transfer between solar wind particles and ionospheric ions, which then lead to the smaller flow velocity shown in our results. Under high P_{dyn} conditions, the solar wind penetrates into lower altitude, thus the discrepancy of ion velocities in the northern hemisphere are eliminated, but remains in low altitude of the southern hemisphere where the strong crustal fields provide additional shielding for the ionosphere. However, since the main driver of the trans-terminator flow remains unclear (Cui et al., 2015; Hamil et al., 2019), the investigation of energy transfer mechanisms responsible for the difference of ion velocity at the terminator region is far beyond the scope of this research.

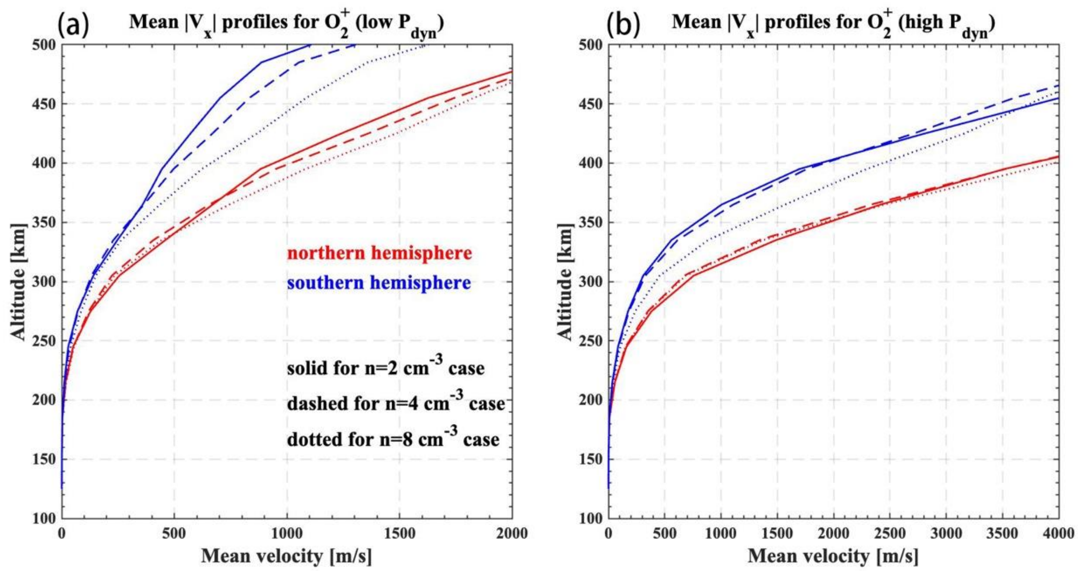

Figure 5. Mean velocity profiles along -X direction for O_2^+ with respect to altitude at XZ plane, divided into the northern (red lines) and the southern (blue lines) hemispheres. Panel a shows cases for low P_{dyn} condition and panel b shows cases for high P_{dyn} condition, with solid, dashed and dotted line represent $\mathrm{n} = 2\ \mathrm{cm}^{-3}$ case, $\mathrm{n} = 4\ \mathrm{cm}^{-3}$ case and $\mathrm{n} = 8\ \mathrm{cm}^{-3}$ case, respectively.

To investigate how solar wind density and velocity influences ion transport more specifically, we analyze the contour plots of plasma speed and ion flux at different iso-surfaces of altitude. Figure 6 depicts the horizontal velocity for O_2^+ in the 350 km altitude plane, presenting color plots of the northward velocity component V_θ and the eastward velocity component V_φ for case 2, with velocity vectors showing the direction of horizontal velocity, as well as the horizontal ion speed for four different cases. On the dayside, the northward velocity V_θ in the northern hemisphere is significantly higher than V_φ as well as the velocity components in the southern hemisphere, similar to the simulation result of Li et al. (2023). Thus, on the northern dayside the horizontal ion flow is generally northward, transporting dayside ionospheric plasma to the nightside ionosphere. The flow pattern in the southern dayside is also less regular as compared to that in the north, indicating that the plasma flow is deflected by the strong crustal fields. This suggests that the southern strong crustal fields cause deceleration and deflection of the horizontal plasma flow in the Martian ionosphere, as reported in previous studies (Li et al., 2022b; Li et al., 2023). In the terminator and near-nightside regions, plasma is flowing towards the nightside, but the magnitude of the velocity is much smaller as compared to that on the northern dayside. Moreover, since the effects of planetary rotation and the Martian wind field are not considered in our model, the horizontal ion flow is generally eastward at dusk and westward at dawn due to the effects of the solar wind and crustal fields. In a more complex model considering rotation and neutral wind, a dawn-dusk asymmetry will be expected to show in the horizontal flow pattern.

In the dayside and terminator region, it is apparent that the magnitude of horizontal velocity V_H is also significantly larger in the northern hemisphere as compared to that in the southern hemisphere, with the highest velocities located on the northern dayside. Therefore, the crustal field hinders both dayside plasma transport and trans-terminator flow, leading to a south-north asymmetry in the flow pattern that influences the nightside ionosphere. The distribution of horizontal velocity also varies significantly for different solar wind condition cases (Figure 6(c)-6(f)). For constant P_{dyn}, the magnitude of V_H in the near terminator region in high n_{sw} cases is larger than that in low n_{sw} cases. On the dayside, the horizontal velocity in the southern hemisphere is slightly lower in high n_{sw} cases than that in low n_{sw} cases, while on the northern dayside the difference is not significant. Comparing the cases of low P_{dyn} and high P_{dyn} conditions, it is obvious that the horizontal velocity is increased significantly with the enhancement of P_{dyn}. Therefore, we deduce that the enhancement of solar wind density is more efficient at accelerating trans-terminator plasma flow as compared to the enhancement of solar wind velocity. Thus, it can be concluded that different solar wind velocity/density conditions influence near-nightside ionosphere by affecting ion velocity and density in the near terminator region.

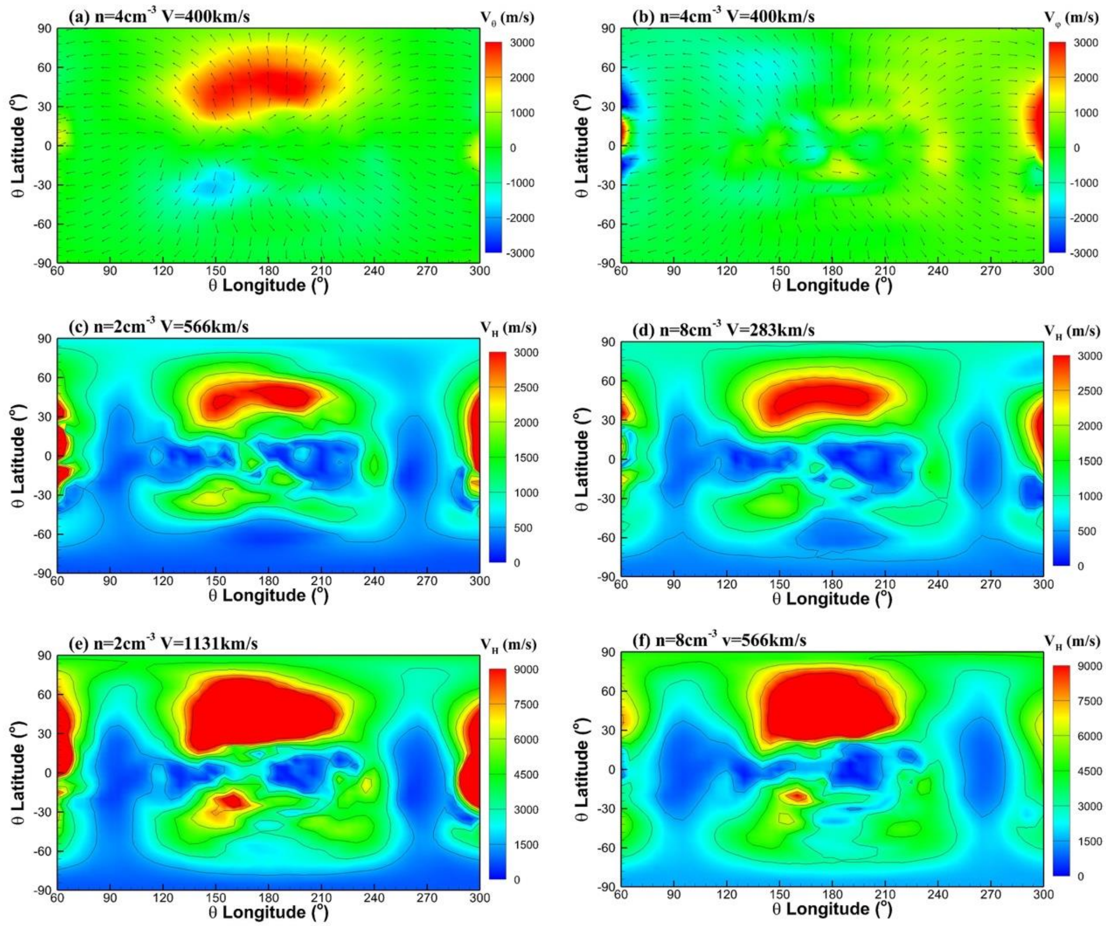

Figure 6. Contour plots of horizontal velocity for O_2^+ at 350 km altitude. Panels a and b show the V_θ, V_φ component for case 2, overlapped with the uniformly presented ion velocity vector (black anchor). Panel c, d, e and f show the horizontal velocity V_H for case 1, case 3, case 4 and case 6, respectively.

The vertical flux of O_2^+ is analyzed to investigate the influence of solar wind density and velocity variation on vertical plasma transport. For low P_{dyn} condition, at 300-350 km altitude, the ion flux is generally flowing inward (downward) at the dayside and near-nightside region, with an outflow (upward) channel being preserved at southern crustal field region. At higher altitudes (400-500 km) outward flow appears in the northern hemisphere. By comparing two of the low P_{dyn} cases presented in Figure 7, it is apparent that high n_{sw} (low V_{sw}) condition result in a higher outward flux and lower inward flux with altitude range 350-500 km, as compared that with low n_{sw} (high V_{sw}) condition, indicating that with constant P_{dyn} condition, decreasing V_{sw} and increasing n_{sw} can promote the ion escape process, leading to a higher escape rate for planetary ions, since a higher V_{sw} will cause a stronger induced magnetic field shielding the ionosphere. Moreover, the stronger inward ion flow in low n_{sw} (high V_{sw}) case drives the ions toward the ground, which leads to the compression of the ionospheric upper boundary presented in Figure 2 and 3. In addition, the outward flow at the southern strong field region is weaker in case 3 as compared to case 1, indicating that for same P_{dyn} condition, increasing n_{sw} while decreasing V_{sw} has suppression effect to the vertical ion outflow channel resulted by crustal field in southern hemisphere.

For high P_{dyn} condition, the outflow flux at the strong crustal field region in the southern hemisphere becomes sporadic as compared to that for low P_{dyn} cases, indicating that the outflow transport channel is partly suppressed in this region. This outflow channel may be mainly provided by the ion escape through vertical magnetic field lines, driven by the ambipolar electric field (Collinson et al., 2019; Li et al., 2022a). Previous studies have shown that the southern hemisphere possesses many vertical field lines to transport heavy ions upward, providing additional ion escape channel (Li et al., 2022a; Weber et al., 2021). Thus, it is reasonable to assume that the outward ion transport channel in the strong crustal field region (shown in Figure 7) is caused by vertical field lines of closed and open magnetic field. High solar wind dynamic pressure compresses the magnetic field structure on the dayside, with lines of draped fields extending to lower altitudes, which will then decrease the presence of closed and open fields at the dayside, and increase the presence of draped fields, resulting in much more horizontal magnetic field morphology (Weber et al., 2019; Xu et al., 2018). Therefore, the outflow channel in this region is partly suppressed under by the enhanced dynamic pressure.

However, except for the region with strong crustal fields, the outward ion flux is significantly enhanced as compared to that of low P_{dyn} cases, contributing to the higher ion escape rate under high P_{dyn}, and the inward flow also decreases at all altitudes, presenting a much more intense depletion effect. Since the ion density in altitude range 300-500 km is decreased for the enhanced P_{dyn} conditions (see Figure 1-3), it can be deduced that the vertical ion velocity experienced an increase along outward direction. As the solar wind penetrates to lower altitudes, the energy transfer from solar wind particles to ionospheric plasma is significantly enhanced, producing more energetic ionospheric ions, which then increases the outflow ion velocity. In this way, the outflow ion flux at topside ionosphere is enhanced greatly.

In addition, the vertical ion flux in the $\mathrm{SZA} > 120°$ region is close to zero at all altitudes and for all solar wind condition cases, indicating that the contribution of deep nightside ($\mathrm{SZA} = 125° - 180°$, defined by Lillis et al. (2009)) ionospheric ion escape to the global escape rate is quite small. Thus, the ion escape flux in the tail region may primarily come from the near-nightside and dayside ionosphere. While investigating how solar wind velocity and density influence ion escape flux, the contribution of deep nightside can be neglected.

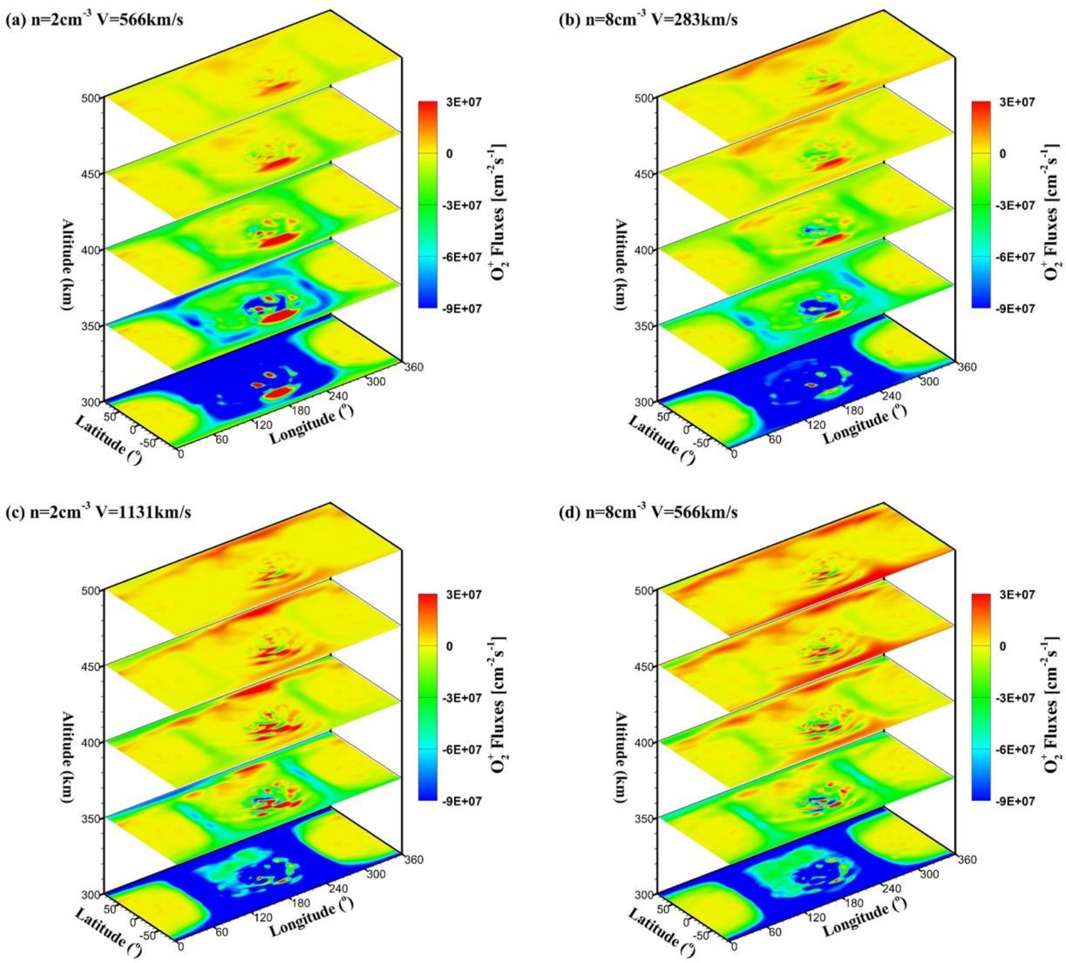

Figure 7. The distribution O_2^+ ion vertical flux with respect to longitude and latitude for multiple altitude slices. Panel a, b, c and d show the result of case 1, case 3, case 4 and case 6, respectively.

4 Discussion and conclusion

In this study, the effects of solar wind density and velocity on the Martian dayside and near-nightside ionosphere, including ion transport at ionospheric altitude, are investigated using 3D multi-fluid MHD simulation models. Our results show that for a given dynamic pressure, different solar wind density and velocity conditions can indeed result in differences within the dayside and near nightside ionosphere, as well as ion transport. The presence of crustal field complicates this process. Comparing our findings to previous observational results (e.g., Fan et al. (2020)), it can be seen that our model results produce the observed ionospheric flow pattern successfully, with the plasma flow being deflected in horizontal direction and enhanced in vertical direction in the southern strong field region.

For constant P_{dyn} conditions, higher n_{sw} can increase the interaction rate between solar wind particles and ionospheric ions and neutrals, leading to an uplifted ionosphere in both the dayside and near-nightside regions. This indicates that a solar wind velocity enhancement event can compress the ionosphere to lower altitude as compared to a solar wind density enhancement event leading to an equivelant rise in the overall dynamic pressure. Through ion transport processes, the nightside ionosphere is also significantly influenced by differing of n_{sw} and V_{sw} conditions. The ion density of the near-nightside ionosphere is much higher for high n_{sw} condition, and the nightside ionospheric ion distribution extends farther into the nightside in this case, indicating stronger day-to-night ion transport. The ion transport velocity also shows apparent distinction under different n_{sw} and V_{sw} condition, accompanied with the differences of ion density distribution to influence ion escape flux. A higher V_{sw} will result in a stronger induced magnetic field through the enhancement of the motional electric field, leading to a stronger shielding of the Martian ionosphere. Thus, the trans-terminator ion velocity and horizontal velocity at ionospheric altitude are higher for low V_{sw} (high n_{sw}) case, since with weaker shielding effect the solar wind particles can penetrate to lower altitude, facilitating energy transfer between solar wind and planetary ions. Moreover, the vertical ion outflow flux is also enhanced for the low V_{sw} (high n_{sw}) case, indicating a higher ion escape rate.

In addition to solar wind velocity and density, our model results also reveal a significant north-south discrepancy for ionospheric structure and plasma transport processes. The ionosphere in the southern hemisphere extends to higher altitudes as compared to that in the northern hemisphere, which can be attributed to the shielding effect of the crustal field and the asymmetry caused by the convention electric field of the solar wind. The trans-terminator flow speed is significantly higher in the northern hemisphere than that in the southern hemisphere, since the strong crustal fields in the southern hemisphere can hinder horizontal ion transport. As a result, in comparison the nightside ionosphere in the northern hemisphere also tends to be more extended into the darkness. The outflow ion flux at topside ionosphere is largely increased on global scale by the enhanced solar wind dynamic pressure, for the compression of the crustal field under high dynamic pressure enhances the depletion effect of solar wind, which then increases the upward ion velocity. Nevertheless, in localized regions, such as those in the vicinity of strong remnant crustal fields, the enhanced solar wind can also suppresses ion outflow by decreasing the presence of vertical magnetic field lines, for ion transport through vertical field lines driven by ambipolar electric field is the main cause of the outflow flux in this region. Thus, the presence of the crustal field also results in an apparent asymmetry of ion outflow.

It should be noted that the MHD model used in this study is an ideal model adopting 1-D neutral density profile. Mechanisms such as neutral wind and dust storm are not included in this model, which may then influence the accuracy of the model at low altitudes. The influences of the asymmetric distributed neutral densities on the Martian plasma environment are excluded. Bougher et al.(2001) indicated that the Martian dayside ionospheric peak is sensitive to the state of the underlying atmosphere, where dust storm can change the O^+ and CO_2^+ density at ionospheric altitude (Qin et al., 2022b). In the absence of these atmospheric processes, the crustal field is the main endogenous source of north-south asymmetry. Therefore, the plasma transport process in the simulation results are significantly simplified compared to the Martian ionosphere which in reality includes atmosphere-thermosphere coupling (e.g., the dawn-dusk asymmetry caused by the rotation of Mars and neutral wind are not shown in our model). In addition, as our model contains only four main species in the Martian ionosphere, some ion species and the correlated chemical reactions that may be important on the nightside are neglected (e.g., NO^+ and HCO^+ (Wu et al., 2019)), which may then increase the discrepancy between the ideal model and the real Martian ionosphere.

Acknowledgments

This work was supported by the National Natural Science Foundation of China (NSFC) under grant No. 42241114, 42074214 and 12150008, and the B-type Strategic Priority Program of the Chinese Academy of Sciences (Grant No. XDB41000000).

Open Research

The MHD simulation data used in the analyses is publicly available online (https://doi.org/10.5281/zenodo.10205974). The data files used in this paper are available at (Song, 2023).

References

Acuña, M. H., Connerney, J. E. P., Wasilewski, P. A., Lin, R. P., Anderson, K. A., Carlson, C. W., ... & Ness, N. F. (1998). Magnetic field and plasma observations at Mars: Initial results of the Mars Global Surveyor mission. *Science*, *279*(5357), 1676-1680. https://doi.org/10.1126/science.284.5415.790

Acuna, M. H., Connerney, J. E. P., Ness, Lin, R. P., Mitchell, D., Carlson, C. W., ... & Cloutier, P. (1999). Global distribution of crustal magnetization discovered by the Mars Global Surveyor MAG/ER experiment. *Science*, *284*(5415), 790-793. https://doi.org/10.1126/science.279.5357.1676

Andrews, D. J., Stergiopoulou, K., Andersson, L., Eriksson, A. I., Ergun, R. E., & Pilinski, M. (2023). Electron densities and temperatures in the Martian ionosphere: MAVEN LPW observations of control by crustal fields. Journal of Geophysical Research: Space Physics, 128(2), e2022JA031027.

Bougher, S. W., Engel, S., Hinson, D. P., & Forbes, J. M. (2001). Mars Global Surveyor radio science electron density profiles: Neutral atmosphere implications. *Geophysical Research Letters*, *28*(16), 3091-3094. https://doi.org/10.1029/2001GL012884

Cao, Y. T., Cui, J., Wu, X. S., Guo, J. P., & Wei, Y. (2019). Structural variability of the nightside martian ionosphere near the terminator: implications on plasma sources. *Journal of Geophysical Research: Planets*, *124*(6), 1495-1511. https://doi.org/10.1029/2019JE005970

Chaufray, J. Y., Gonzalez-Galindo, F., Forget, F., Lopez-Valverde, M., Leblanc, F., Modolo, R., ... & Witasse, O. (2014). Three-dimensional Martian ionosphere model: II. Effect of transport processes due to pressure gradients. *Journal of Geophysical Research: Planets*, *119*(7), 1614-1636. https://doi.org/10.1002/2013JE004551

Chu, F., Girazian, Z., Gurnett, D. A., Morgan, D. D., Halekas, J., Kopf, A. J., ... & Duru, F. (2019). The effects of crustal magnetic fields and solar EUV flux on ionopause formation at Mars. *Geophysical Research Letters*, *46*(17-18), 10257-10266. https://doi.org/10.1029/2021JE006936

Chu, F., Girazian, Z., Duru, F., Ramstad, R., Halekas, J., Gurnett, D. A., ... & Kopf, A. J. (2021). The dayside ionopause of Mars: Solar wind interaction, pressure balance, and comparisons with Venus. *Journal of Geophysical Research: Planets*, *126*(11), e2021JE006936. https://doi.org/10.1029/2021JE006936

Collinson, G., Glocer, A., Xu, S., Mitchell, D., Frahm, R. A., Grebowsky, J., ... & Jakosky, B. (2019). Ionospheric ambipolar electric fields of Mars and Venus: Comparisons between theoretical predictions and direct observations of the electric potential drop. *Geophysical research letters*, *46*(3), 1168-1176. https://doi.org/10.1029/2018GL080597

Connerney, J. E., Espley, J. R., DiBraccio, G. A., Gruesbeck, J. R., Oliversen, R. J., Mitchell, D. L., ... & Jakosky, B. M. (2015). First results of the MAVEN magnetic field investigation. *Geophysical Research Letters, 42*(21), 8819-8827. https://doi.org/10.1002/2015GL065366

Cui, J., Galand, M., Yelle, R. V., Wei, Y., & Zhang, S. J. (2015). Day-to-night transport in the Martian ionosphere: Implications from total electron content measurements. *Journal of Geophysical Research: Space Physics*, *120*(3), 2333-2346. https://doi.org/10.1002/2014JA020788

Cui, J., Cao, Y. T., Wu, X. S., Xu, S. S., Yelle, R. V., Stone, S., ... & Wei, Y. (2019). Evaluating local ionization balance in the nightside Martian upper atmosphere during MAVEN Deep Dip campaigns. *The Astrophysical Journal Letters*, *876*(1), L12. https://doi.org/10.3847/2041-8213/ab1b34

Diéval, C., Morgan, D. D., Němec, F., & Gurnett, D. A. (2014). MARSIS observations of the Martian nightside ionosphere dependence on solar wind conditions. *Journal of Geophysical Research: Space Physics*, *119*(5), 4077-4093. https://doi.org/10.1002/2014JA019788

Dong, C., Bougher, S. W., Ma, Y., Toth, G., Nagy, A. F., & Najib, D. (2014). Solar wind interaction with Mars upper atmosphere: Results from the one-way coupling between the multifluid MHD model and the MTGCM model. *Geophysical Research Letters*, *41*(8), 2708-2715. https://doi.org/10.1002/2014GL059515

Dong, C., Ma, Y., Bougher, S. W., Toth, G., Nagy, A. F., Halekas, J. S., ... & Grebowsky, J. M. (2015). Multifluid MHD study of the solar wind interaction with Mars' upper atmosphere during the 2015 March 8th ICME event. *Geophysical Research Letters*, *42*(21), 9103-9112. https://doi.org/10.1002/2015GL065944

Dubinin, E., Fränz, M., Pätzold, M., McFadden, J., Halekas, J. S., Connerney, J. E. P., ... & Zelenyi, L. (2018). Martian ionosphere observed by MAVEN. 3. Influence of solar wind and IMF on upper ionosphere. *Planetary and Space Science*, *160*, 56-65. https://doi.org/10.1016/j.pss.2018.03.016

Dubinin, E., Fränz, M., Pätzold, M., Woch, J., McFadden, J., Halekas, J. S., ... & Zelenyi, L. (2019). Expansion and shrinking of the Martian topside ionosphere. *Journal of Geophysical Research: Space Physics*, *124*(11), 9725-9738. https://doi.org/10.1029/2019JA027077

Duru, F., Gurnett, D. A., Frahm, R. A., Winningham, J. D., Morgan, D. D., & Howes, G. G. (2009). Steep, transient density gradients in the Martian ionosphere similar to the ionopause at Venus. *Journal of Geophysical Research: Space Physics*, *114*(A12). https://doi.org/10.1029/2009JA014711

Duru, F., Baker, N., De Boer, M., Chamberlain, A., Verchimak, R., Morgan, D. D., ... & Kopf, A. (2020). Martian ionopause boundary: Coincidence with photoelectron boundary and response to internal and external drivers. *Journal of Geophysical Research: Space Physics*, *125*(5), e2019JA027409. https://doi.org/10.1029/2019JA027409

Edberg, N. J. T., Brain, D. A., Lester, M., Cowley, S. W. H., Modolo, R., Fränz, M., & Barabash, S. (2009, September). Plasma boundary variability at Mars as observed by Mars Global Surveyor and Mars Express. In *Annales Geophysicae* (Vol. 27, No. 9, pp. 3537-3550). Göttingen, Germany: Copernicus Publications. https://doi.org/10.5194/angeo-27-3537-2009

Edberg, N. J. T., Nilsson, H., Williams, A. O., Lester, M., Milan, S. E., Cowley, S. W. H., ... & Futaana, Y. (2010). Pumping out the atmosphere of Mars through solar wind pressure pulses. *Geophysical Research Letters, 37*(3). https://doi.org/10.1029/2009GL041814

Fang, X., Ma, Y., Masunaga, K., Dong, Y., Brain, D., Halekas, J., ... & Dong, C. (2017). The Mars crustal magnetic field control of plasma boundary locations and atmospheric loss: MHD prediction and comparison with MAVEN. *Journal of Geophysical Research: Space Physics, 122*(4), 4117-4137. https://doi.org/10.1002/2016JA023509

Flynn, C. L., Vogt, M. F., Withers, P., Andersson, L., England, S., & Liu, G. (2017). MAVEN observations of the effects of crustal magnetic fields on electron density and temperature in the Martian dayside ionosphere. Geophysical Research Letters, 44(21), 10-812.

Fowler, C. M., Andersson, L., Ergun, R. E., Morooka, M., Delory, G., Andrews, D. J., ... & Jakosky, B. M. (2015). The first in situ electron temperature and density measurements of the Martian nightside ionosphere. *Geophysical Research Letters*, *42*(21), 8854-8861. https://doi.org/10.1002/2015GL065267

Gao, J. W., Rong, Z. J., Klinger, L., Li, X. Z., Liu, D., & Wei, Y. (2021). A spherical harmonic Martian crustal magnetic field model combining data sets of MAVEN and MGS. *Earth and Space Science*, *8*(10), e2021EA001860. https://doi.org/10.1029/2021EA001860

Garnier, P., Steckiewicz, M., Mazelle, C., Xu, S., Mitchell, D., Holmberg, M. K. G., ... & Jakosky, B. M. (2017). The Martian photoelectron boundary as seen by MAVEN. *Journal of Geophysical Research: Space Physics*, *122*(10), 10-472. https://doi.org/10.1002/2017JA024497

Garnier, P., Jacquey, C., Gendre, X., Génot, V., Mazelle, C., Fang, X., ... & Halekas, J. S. (2022). The drivers of the Martian bow shock location: A statistical analysis of Mars

Atmosphere and Volatile EvolutioN and Mars Express observations. *Journal of Geophysical Research: Space Physics*, *127*(5), e2021JA030147. https://doi.org/10.1029/2021JA030147

Girazian, Z., Mahaffy, P., Lillis, R. J., Benna, M., Elrod, M., Fowler, C. M., & Mitchell, D. L. (2017). Ion densities in the nightside ionosphere of Mars: Effects of electron impact ionization. *Geophysical Research Letters*, *44*(22), 11-248. https://doi.org/10.1002/2017GL075431

Girazian, Z., Halekas, J., Morgan, D. D., Kopf, A. J., Gurnett, D. A., & Chu, F. (2019). The effects of solar wind dynamic pressure on the structure of the topside ionosphere of Mars. *Geophysical Research Letters*, *46*(15), 8652-8662. https://doi.org/10.1029/2019GL083643

Hamil, O., Cravens, T. E., Rahmati, A., Connerney, J. E. P., & Andersson, L. (2019). Pressure gradients driving ion transport in the topside Martian atmosphere. *Journal of Geophysical Research: Space Physics*, *124*(7), 6117-6126. https://doi.org/10.1029/2019JA026670

Harada, Y., Gurnett, D. A., Kopf, A. J., Halekas, J. S., Ruhunusiri, S., DiBraccio, G. A., ... & Brain, D. A. (2018). MARSIS observations of the Martian nightside ionosphere during the September 2017 solar event. *Geophysical Research Letters*, *45*(16), 7960-7967. https://doi.org/10.1002/2018GL077622

Harnett, E. M., & Winglee, R. M. (2003). The influence of a mini-magnetopause on the magnetic pileup boundary at Mars. *Geophysical Research Letters*, *30*(20). https://doi.org/10.1029/2003GL017852

Harnett, E. M., & Winglee, R. M. (2005). Three-dimensional fluid simulations of plasma asymmetries in the Martian magnetotail caused by the magnetic anomalies. *Journal of Geophysical Research: Space Physics*, *110*(A7). https://doi.org/10.1029/2003JA010315

Intriligator, D. S., & Smith, E. J. (1979). Mars in the solar wind. *Journal of Geophysical Research: Solid Earth*, *84*(B14), 8427-8435. https://doi.org/10.1029/JB084iB14p08427

Kaneda, K., Terada, N., & Machida, S. (2007). Time variation of nonthermal escape of oxygen from Mars after solar wind dynamic pressure enhancement. *Geophysical research letters*, *34*(20). https://doi.org/10.1029/2007GL030576

Ledvina, S. A., Ma, Y. J., & Kallio, E. (2008). Modeling and simulating flowing plasmas and related phenomena. *Space Science Reviews*, *139*, 143-189. https://doi.org/10.1007/s11214-008-9384-6

Li, G., Lu, H., Li, Y., CAO, J. B., & Li, S. (2023). Influence of the Martian crustal magnetic fields on the Mars-solar wind interaction and plasma transport. *Frontiers in Astronomy and Space Sciences*, *10*, 113. https://doi.org/10.3389/fspas.2023.1162005

Li, S., Lu, H., Cui, J., Yu, Y., Mazelle, C., Li, Y., & Cao, J. (2020). Effects of a dipole-like crustal field on solar wind interaction with Mars. *Earth and Planetary Physics*, *4*(1), 23-31. https://doi.org/10.26464/epp2020005

Li, S., Lu, H., Cao, J., Mazelle, C., Cui, J., Rong, Z., ... & Li, G. (2022a). The Impact and Mechanism of the Magnetic Inclination Angle on O+ Escape from Mars. *The Astrophysical Journal*, *931*(1), 30. https://doi.org/10.3847/1538-4357/ac6510

Li, S., Lu, H., Cao, J., Cui, J., Zhou, C., Wild, J. A., ... & Li, Y. (2022b). Deflection of O2+ Ion Flow by Magnetic Fields in the Martian Ionosphere. *The Astrophysical Journal*, *941*(2), 198. https://doi.org/10.3847/1538-4357/aca32b

Lillis, R. J., Fillingim, M. O., Peticolas, L. M., Brain, D. A., Lin, R. P., & Bougher, S. W. (2009). Nightside ionosphere of Mars: Modeling the effects of crustal magnetic fields and electron pitch angle distributions on electron impact ionization. *Journal of Geophysical Research: Planets*, *114*(E11). https://doi.org/10.1029/2009JE003379

Ma, Y., Nagy, A. F., Sokolov, I. V., & Hansen, K. C. (2004). Three-dimensional, multispecies, high spatial resolution MHD studies of the solar wind interaction with Mars. *Journal of Geophysical Research: Space Physics*, *109*(A7). https://doi.org/10.1029/2003JA010367

Ma, Y. J., Fang, X., Nagy, A. F., Russell, C. T., & Toth, G. (2014). Martian ionospheric responses to dynamic pressure enhancements in the solar wind. *Journal of Geophysical Research: Space Physics*, *119*(2), 1272-1286. https://doi.org/10.1002/2013JA019402

Ma, Y. J., Russell, C. T., Fang, X., Dong, C. F., Nagy, A. F., Toth, G., ... & Jakosky, B. M. (2017). Variations of the Martian plasma environment during the ICME passage on 8 March 2015: A time-dependent MHD study. *Journal of Geophysical Research: Space Physics*, *122*(2), 1714-1730. https://doi.org/10.1002/2016JA023402

Nagy, A. F., Winterhalter, D., Sauer, K., Cravens, T. E., Brecht, S., Mazelle, C., ... & Trotignon, J. G. (2004). The plasma environment of Mars. *Mars' magnetism and its interaction with the solar wind*, 33-114. https://doi.org/10.1007/978-0-306-48604-3_2

Najib, D., Nagy, A. F., Tóth, G., & Ma, Y. (2011). Three-dimensional, multifluid, high spatial resolution MHD model studies of the solar wind interaction with Mars. *Journal of Geophysical Research: Space Physics*, *116*(A5). https://doi.org/10.1029/2010JA016272

Němec, F., Morgan, D. D., Gurnett, D. A., & Duru, F. (2010). Nightside ionosphere of Mars: Radar soundings by the Mars Express spacecraft. *Journal of Geophysical Research: Planets*, *115*(E12). https://doi.org/10.1029/2010JE003663

Qin, J., Zou, H., Ye, Y., Hao, Y., & Wang, J. (2022a). A denser and elevated Martian nightside ionosphere during Mars season Ls 180–360°. *Icarus*, *388*, 115255. https://doi.org/10.1016/j.icarus.2022.115255

Qin, J., Zou, H., Lee, Y., Ye, Y., Hao, Y., & Wang, J. (2022b). Effect of the 2018 Martian global dust storm on the main species in the upper ionosphere: observations and simulations. *Journal of Geophysical Research: Planets*, *127*(7), e2022JE007297. https://doi.org/10.1029/2022JE007297

Ramstad, R., Barabash, S., Futaana, Y., Nilsson, H., Wang, X. D., & Holmström, M. (2015). The Martian atmospheric ion escape rate dependence on solar wind and solar EUV conditions: 1. Seven years of Mars Express observations. *Journal of Geophysical Research: Planets*, *120*(7), 1298-1309. https://doi.org/10.1002/2015JE004816

Ramstad, R., Barabash, S., Futaana, Y., Nilsson, H., & Holmström, M. (2017). Global Mars-solar wind coupling and ion escape. *Journal of Geophysical Research: Space Physics*, *122*(8), 8051-8062. https://doi.org/10.1002/2017JA024306

Ramstad, R., Brain, D. A., Dong, Y., Espley, J., Halekas, J., & Jakosky, B. (2020). The global current systems of the Martian induced magnetosphere. *Nature Astronomy*, *4*(10), 979-985. https://doi.org/10.1038/s41550-020-1099-y

Sánchez-Cano, B., Narvaez, C., Lester, M., Mendillo, M., Mayyasi, M., Holmstrom, M., ... & Durward, S. (2020). Mars' ionopause: A matter of pressures. *Journal of Geophysical Research: Space Physics*, *125*(9), e2020JA028145. https://doi.org/10.1029/2020JA028145

Song, Y. (2023). Effects of solar wind density and velocity variations on the Martian ionosphere and plasma transport-a MHD model study [Dataset]. Zenodo. https://doi.org/10.5281/zenodo.10205974

Song, Y., Lu, H., Cao, J., Li, S., Yu, Y., Wang, S., ... & Wang, J. (2023). Effects of Force in the Martian Plasma Environment with Solar Wind Dynamic Pressure Enhancement. *Journal of Geophysical Research: Space Physics*, e2022JA031083. https://doi.org/10.1029/2022JA031083

Stergiopoulou, K., Andrews, D. J., Edberg, N. J., Halekas, J., Lester, M., Sánchez-Cano, B., ... & Gruesbeck, J. R. (2022). A Two-Spacecraft Study of Mars' Induced Magnetosphere's Response to Upstream Conditions. *Journal of Geophysical Research: Space Physics*, *127*(4), e2021JA030227. https://doi.org/10.1029/2021JA030227

Vogt, M. F., Withers, P., Mahaffy, P. R., Benna, M., Elrod, M. K., Halekas, J. S., ... & Jakosky, B. M. (2015). Ionopause-like density gradients in the Martian ionosphere: A first look with MAVEN. *Geophysical Research Letters*, *42*(21), 8885-8893. https://doi.org/10.1002/2015GL065269

Wang, M., Xie, L., Lee, L. C., Xu, X. J., Kabin, K., Lu, J. Y., ... & Li, L. (2020). A 3D parametric martian bow shock model with the effects of mach number, dynamic pressure, and the interplanetary magnetic field. *The Astrophysical Journal*, *903*(2), 125. https://doi.org/10.3847/1538-4357/abbc04

Wang, M., Lee, L. C., Xie, L., Xu, X., Lu, J. Y., Kabin, K., ... & Sui, H. Y. (2021). Effect of solar wind density and velocity on the subsolar standoff distance of the Martian magnetic pileup boundary. *Astronomy & Astrophysics*, *651*, A22. https://doi.org/10.1051/0004-6361/202140511

Weber, T., Brain, D., Mitchell, D., Xu, S., Espley, J., Halekas, J., ... & Jakosky, B. (2019). The influence of solar wind pressure on Martian crustal magnetic field topology. *Geophysical Research Letters*, *46*(5), 2347-2354. https://doi.org/10.1029/2019GL081913

Weber, T., Brain, D., Xu, S., Mitchell, D., Espley, J., Mazelle, C., ... & Jakosky, B. (2021). Martian crustal field influence on O+ and O2+ escape as measured by MAVEN. *Journal of*

Geophysical Research: Space Physics, *126*(8), e2021JA029234. https://doi.org/10.1029/2021JA029234

Withers, P. (2009). A review of observed variability in the dayside ionosphere of Mars. *Advances in Space Research*, *44*(3), 277-307. https://doi.org/10.1016/j.asr.2009.04.027

Withers, P., Fillingim, M. O., Lillis, R. J., Häusler, B., Hinson, D. P., Tyler, G. L., ... & Witasse, O. (2012a). Observations of the nightside ionosphere of Mars by the Mars Express radio science experiment (MaRS). *Journal of Geophysical Research: Space Physics*, *117*(A12). https://doi.org/10.1029/2012JA018185

Withers, P., Fallows, K., Girazian, Z., Matta, M., Häusler, B., Hinson, D., ... & Witasse, O. (2012b). A clear view of the multifaceted dayside ionosphere of Mars. *Geophysical Research Letters*, *39*(18). https://doi.org/10.1029/2012GL053193

Withers, P., Flynn, C. L., Vogt, M. F., Mayyasi, M., Mahaffy, P., Benna, M., ... & England, S. (2019). Mars's dayside upper ionospheric composition is affected by magnetic field conditions. Journal of Geophysical Research: Space Physics, 124(4), 3100-3109.

Wu, X. S., Cui, J., Xu, S. S., Lillis, R. J., Yelle, R. V., Edberg, N. J., ... & Mitchell, D. L. (2019). The morphology of the topside Martian ionosphere: Implications on bulk ion flow. *Journal of Geophysical Research: Planets*, *124*(3), 734-751. https://doi.org/10.1029/2018JE005895

Xu, S., Fang, X., Mitchell, D. L., Ma, Y., Luhmann, J. G., DiBraccio, G. A., ... & Lee, C. O. (2018). Investigation of Martian magnetic topology response to 2017 September ICME. *Geophysical Research Letters*, *45*(15), 7337-7346. https://doi.org/10.1029/2018GL077708

Zhang, M. H. G., Luhmann, J. G., & Kliore, A. J. (1990). An observational study of the nightside ionospheres of Mars and Venus with radio occultation methods. *Journal of Geophysical Research: Space Physics*, *95*(A10), 17095-17102. https://doi.org/10.1029/JA095iA10p17095